






ORIGINAL ARTICLE

HNF1B-driven three-dimensional chromatin structure for molecular classification in pancreatic cancers

Hiroyuki Kato¹  | Keisuke Tateishi^{1,2}  | Dosuke Iwadate¹ | Keisuke Yamamoto¹  | Hiroaki Fujiwara^{1,3} | Takuma Nakatsuka¹ | Yotaro Kudo¹  | Yoku Hayakawa¹  | Hideaki Ijichi¹ | Motoyuki Otsuka¹ | Takahiro Kishikawa¹ | Ryota Takahashi¹ | Koji Miyabayashi¹ | Yousuke Nakai^{1,4} | Yoshihiro Hirata⁵ | Atsushi Toyoda⁶ | Shinichi Morishita⁷ | Mitsuhiro Fujishiro¹

¹Department of Gastroenterology, Graduate School of Medicine, The University of Tokyo, Tokyo, Japan

²Division of Gastroenterology, Department of Internal Medicine, St Marianna University School of Medicine, Kawasaki, Japan

³Division of Gastroenterology, The Institute of Medical Science, Asahi Life Foundation, Tokyo, Japan

⁴Department of Endoscopy and Endoscopic Surgery, The University of Tokyo Hospital, Tokyo, Japan

⁵Division of Advanced Genome Medicine, The Institute of Medical Science, The University of Tokyo, Tokyo, Japan

⁶Comparative Genomics Laboratory, National Institute of Genetics, Shizuoka, Japan

⁷Department of Computational Biology and Medical Sciences, Graduate School of Frontier Sciences, The University of Tokyo, Chiba, Japan

Correspondence

Keisuke Tateishi, Division of Gastroenterology, Department of Internal Medicine, St Marianna University School of Medicine, 2-16-1 Sugao, Miyamae-ku, 216-8511, Kawasaki, Kanagawa, Japan. Email: ktatetky@gmail.com

Funding information

MSD Life Science Foundation, Public Interest Incorporated Foundation; The International Joint Usage/Research Center, Institute of Medical Science, the University of Tokyo; Tokyo Society of Medical Science; Yasuda Memorial Medical Foundation; Japan Society for the Promotion of Science, Grant/Award Number: 16H06279 (PAGS), 19K08435, 21K15966, 21K20828, 22H02898 and 22H03053; Uehara Memorial Foundation; Takeda Science Foundation; Yasuda Medical Foundation; Astellas Foundation for Research on Metabolic Disorders; Princess Takamatsu Cancer Research Fund; Life Science Foundation of Japan; International Joint Usage/Research Center, the Institute of Medical Science,

Abstract

The molecular subtypes of pancreatic cancer (PC), either classical/progenitor-like or basal/squamous-like, are currently a major topic of research because of their direct association with clinical outcomes. Some transcription factors (TFs) have been reported to be associated with these subtypes. However, the mechanisms by which these molecular signatures of PCs are established remain unknown. Epigenetic regulatory processes, supported by dynamic changes in the chromatin structure, are essential for transcriptional profiles. Previously, we reported the importance of open chromatin profiles in the biological features and transcriptional status of PCs. Here, we aimed to analyze the relationships between three-dimensional (3D) genome structures and the molecular subtypes of human PCs using Hi-C analysis. We observed a correlation of the specific elements of 3D genome modules, including compartments, topologically associating domains, and enhancer-promoter loops, with the expression of related genes. We focused on HNF1B, a TF that is implicated in the progenitor subtype. Forced expression of HNF1B in squamous-type PC organoids induced the upregulation and downregulation of genes associated with progenitor and squamous subtypes, respectively. Long-range genomic interactions induced by HNF1B were accompanied

Abbreviations: E-P, enhancer-promoter; GSEA, gene set enrichment analysis; IDR, intrinsically disordered region; IPMN, intraductal papillary mucinous neoplasm; IPMNiv, invasive intraductal papillary mucinous neoplasm; OE, overexpression; PC, pancreatic cancer; PDAC, pancreatic ductal adenocarcinoma; PG, progenitor; SQ, squamous; 3D, three-dimensional; TAD, topologically associating domain; TF, transcriptional factor.

This is an open access article under the terms of the [Creative Commons Attribution-NonCommercial-NoDerivs](https://creativecommons.org/licenses/by-nc-nd/4.0/) License, which permits use and distribution in any medium, provided the original work is properly cited, the use is non-commercial and no modifications or adaptations are made.

© 2022 The Authors. *Cancer Science* published by John Wiley & Sons Australia, Ltd on behalf of Japanese Cancer Association.

the University of Tokyo

by compartment modulation and H3K27ac redistribution. We also found that these HNF1B-induced changes in subtype-related gene expression required an intrinsically disordered region, suggesting a possible involvement of phase separation in compartment modulation. Thus, mapping of 3D structural changes induced by TFs, such as HNF1B, may become a useful resource for further understanding the molecular features of PCs.

KEYWORDS

Hi-C, HNF1B, intrinsically disordered region, pancreatic cancer, patient-derived organoid

1 | INTRODUCTION

Research based on large patient datasets has suggested that pancreatic cancer (PC) can be divided into two transcriptional subtypes: classical/progenitor-like (PG) and basal/squamous-like (SQ).¹⁻⁴ These subtypes are directly linked to patient outcomes and are thus the subject of PC research.⁵⁻⁷ The subtypes express specific transcriptional factors (TFs), such as GATA6, FOXA2, HNF1B, and HNF4A, in the PG type and TP63 and SIX4 in the SQ type.³⁻⁹ However, the mechanisms by which these TFs dynamically regulate their respective molecular signatures remain unclear.

The two pathological types of PC, pancreatic ductal adenocarcinoma (PDAC) and invasive intraductal papillary mucinous neoplasm (IPMN_{inv}), are derived from different precursors: pancreatic intraepithelial neoplasm (PanIN)¹⁰ and IPMN.¹¹ IPMN_{inv} often tends to be the PG subtype.³ We previously analyzed chromatin profiles by assay for transposase-accessible chromatin with high-throughput sequencing (ATAC-seq) in PCs, especially IPMN lineages, and clarified close relationships of chromatin accessibility and biological features.¹² The importance of three-dimensional (3D) genome structures in cell type determination and disease characterization has recently been discovered.¹³⁻¹⁸ Therefore, we attempted to address how 3D genome structures play a role in PCs using Hi-C analysis. 3D genome structures are organized in a hierarchy of various module layers, including compartments, topologically associating domains (TADs), and DNA loops. Briefly, the genome is spatially segregated into two compartments, A and B, which encompass transcriptionally active and inactive regions, respectively.¹⁹ TADs are self-interacting domains that are genome segments of approximately 1 Mb in size and are insulated by the CCCTC-binding factor (CTCF).²⁰ Chromatin interaction within TADs often forms a DNA loop structure, thereby linking promoters to regulatory elements, such as enhancers, to establish a transcription complex (enhancer-promoter [E-P] loop).^{21,22} Growing evidence indicates that compartments and TADs are formed via distinct mechanisms.²³ The role of the CTCF and cohesin complex in TAD and loop formation has been well studied,^{24,25} whereas compartments have been proposed to be established according to local chromatin states.²⁶ Recently, TF-induced phase-separating condensate, a nonmembranous organelle concentrating proteins and nucleic acids to assemble transcription machinery driven by polar and charged amino acids of the intrinsically disordered region

(IDR) of TFs, has emerged as a mechanism to establish compartment profiles; it has become a topic for elucidating the biology of cancer phenotypes or drug sensitivities.²⁷⁻³¹

Here, we propose the possible involvement of 3D genome structures in the transcriptional subtypes of PC. Our data using Hi-C analysis demonstrated that the "switch" of subtype gene signature induced by HNF1B, a characteristic PG-type TF, was followed by the alteration of 3D genome structures. The IDR of the HNF1B protein was required for the expression of subtype-specific genes, suggesting a possible involvement of the alteration of genomic compartments. This study suggests that TF-induced 3D chromatin remodeling offers a new field for understanding the molecular features of PC.

2 | MATERIALS AND METHODS

2.1 | Organoid cultures

The organoids were cultured with Matrigel (Corning) coating, supplied with complete media every 4 days, and incubated at 5% CO₂ in 20% O₂. The complete medium was prepared as previously described.¹² Briefly, advanced Dulbecco's modified Eagle's Medium/F12 (Thermo Fisher Scientific) (40%), with 10 mM HEPES (Thermo Fisher Scientific), 1 × GlutaMAX (Thermo Fisher Scientific), Wnt3a conditioned medium (ATCC® CRL2647™) (50%), and R-spondin1 conditioned medium (10%)³² was supplemented with 100 μg/mL primocin (InvivoGen), 1 × B27 (Thermo Fisher Scientific), 10 nM gastrin I (Sigma), 1 mM N-acetylcysteine (Wako), 10 mM Nicotinamide (Sigma), 50 ng/ml human recombinant EGF (Thermo Fisher Scientific), 100 ng/ml human recombinant FGF10 (Peprotech), 100 ng/ml human recombinant noggin (Peprotech), and 500 nM A83-01 (Tocris). A total of 10 μM Y-27632 (Fujifilm Wako) was supplemented when passaging.

2.2 | Hi-C

One million cells from organoids were cross-linked with 2% formaldehyde for 10 minutes at room temperature and were quenched using stop solution. The library was prepared using the Arima Hi-C kit (Arima Genomics) according to the manufacturer's instructions and sequenced by NovaSeq6000 (Illumina) with paired-end 150 bp

reads. Reads were processed with the Juicer pipeline,³³ and KR normalization was used unless otherwise noted.

Global contact matrix correlation between each sample was calculated by HiCRep.³⁴ Stratum-adjusted correlation coefficient (SCC) was calculated in each of chromosomes 1-22 and X at a resolution of 1 Mb, and median SCC value was used to generalize the correlation between the samples. For compartment analysis, we used Calder algorithm at 50kb resolution to enable continuous scoring for each subcompartment.³⁵ We also presented the eigenvector value with gene-enriched regions being annotated as compartment A (positive eigenvector value). TADs were called using normalized 50kb resolution contact matrices through Hi-C explorer with default parameters.³⁶ To define common and specific TAD borders, borders were expanded one bin (50kb) on each side and were determined as common borders if they overlapped between samples. We calculated TAD domain score as reported previously.¹⁷ First, we extracted "intra-TAD contacts" by taking the sum of the KR-normalized interaction within the TAD. Only common TADs among the comparisons (3634 TADs between IPMNiv2 and PDAC1; 3903 TADs among HNF1B overexpression [OE] experiments) were used. Next, each TAD's "intra-TAD contact" was further divided by the sum of each TAD's "intra+inter-TAD contact," yielding the TAD domain score of that TAD. To calculate log₂ fold change, we first converted domain score, which ranges from 0 to 1, to three-digit integer using "ROUND" function. These integers were used as input for edgeR³⁷ (comparison between IPMNiv2 and PDAC1) or DESeq2³⁸ (comparison in HNF1B^{OE} experiments).

Loops were called using HiCCUPS,³³ and those located on chromosomes 1-22 and X were considered. Significant differential loops were further called by HiCCUPSDiff.³³ We used pgltools to identify overlap and specificity of the loops.³⁹ Loops were further filtered to only those whose anchors matched enhancers and promoters. Enhancers are defined as merged set of H3K27ac chromatin immunoprecipitation sequencing (ChIP-seq) peaks in IPMNiv2 and PDAC1 (72,242 peaks) (E-GEAD-417). Promoters are defined as transcription start site (TSS) ± 1kb. E-P loop interactions were calculated by extracting KR-normalized contacts. We also used HiC-DC+ (5kb resolution) for differential loop interaction comparison in HNF1B^{OE} experiments.⁴⁰ As multiple loops could be called per gene, we took into account the ones that exhibited changes most likely to have contributed to their gene expression difference for heatmap presentation. Virtual 4C plot was created from Juicebox.⁴¹ We first chose a viewpoint region, namely, bins containing TSS of GATA6 (chr18: 19,750-19,755kb) and then extracted the KR-normalized Hi-C matrix at 5kb resolution. FitHiC was performed at 5kb resolution with cutoff set to false discovery rate (FDR) < 0.05.⁴² To integrate gene expression, each gene was allocated to genome modules based on its TSS location. Hi-C sequences could be affected by copy number variations (CNVs). Indeed, the compartment scores and E-P interactions were positively biased and domain scores were negatively biased to CNVs. Therefore, we adjusted RNA values based on the CNV status when comparing IPMNiv2 and PDAC1.

To investigate which of the 3D genome modules particularly associated with subtype gene expression, we assigned each gene to

each 3D module that had the strongest difference (log₂ fold change) between the cell types. Heatmap was presented as to clarify positive and negative values, and 3D modules that were not annotated in the indicated gene were colored gray.

To analyze the long-range contacts between HNF1B targeting sites, we used PE-SCAN⁴³ to determine if the combination of the two regions that are > 5 Mb apart are in closer contact than expected. The results are shown as submatrices of the log₂(observed/expected) at 10kb resolution between pairs of HNF1B peaks within the range of 250kb up- and downstream. The top 2500 HNF1B ChIP-seq signal peaks were used as a reference for HNF1B-targeting sites. Saddle plots and compartment strength were calculated using Genome Organisation Visual Analytics (GENOVA) software at 50kb resolution.⁴⁴

2.3 | Mutagenesis of HNF1B IDR

Open reading frame of HNF1B was cloned into pLVISIN-EF1 α Hyg Vector (Takara). HNF1B-dIDR (IDR deleted) mutant was cloned by inverse PCR using the KOD -Plus- Mutagenesis Kit (Toyobo). AKAP95 (amino acid 101-210) was cloned from cDNA of 293 T cells and was inserted into HNF1B-dIDR plasmid using Gibson Assembly Master Mix (NEB). PCR primers are listed in Table S1. All the coding regions were sequence verified.

2.4 | Overexpression experiments

Lentivirus was produced using psPAX2 (Addgene, #12260) and pMD2.G (Addgene, #12259), followed by virus concentration using Amicon Ultra 100k (Millipore). Lentivirus transfection to organoids was performed using the spin inoculation method. Briefly, organoids dissociated into single cells were plated onto a 48-well plate with 120 μ l complete medium, 15 μ l of concentrated virus, and 8 μ g/ml polybrene. The plate was centrifuged at 600 g for 60 minutes at 32°C, followed by 6 hours culture at 37°C, washed, and then seeded with Matrigel embedding. Transfected cells were selected with 100 μ g/ml hygromycin. Downstream sequencing experiments (RNA-seq, ChIP-seq, and Hi-C) were performed together with the empty vector control whose culture period and passage times are managed to be the same. Number of colonies that formed ductal-like structures shown in Figure S4C were counted per each well 3 days after seeding 2×10^5 cells into a six-well plate.

2.5 | Western blot analysis

Western blot analysis was performed as previously described.¹² Whole-cell lysates of organoids were prepared by lysing with RIPA buffer. The lysates were further sonicated for 5 minutes and centrifuged, and the supernatants were collected. These lysates were separated by SDS-PAGE, followed by immunoblotting using primary antibodies listed in Table S2. All images were taken using LuminoGraph (Atto).

2.6 | Immunofluorescence

A total of 5×10^4 cells were seeded onto a four-well chamber slide (Thermo Fisher Scientific) and cultured for 2 days. Cells were then fixed with 2% PFA/PBS for 10 minutes at RT, permeabilized with 0.25% TritonX-100/PBS for 15 minutes at RT, blocked with 5% goat serum/PBS for 1 hour at RT, and then incubated with HNF1B antibody (Sigma, HPA002083) diluted in 5% serum/PBS and incubated overnight at 4°C. Slides were then incubated with fluorescence-conjugated secondary antibody (Table S2). Nuclei were labeled using Hoechst. Images were taken using DMI8 (Leica).

2.7 | RNA-seq

RNA was extracted from organoids using the RNeasy Micro Kit (Qiagen). Libraries were prepared using the TruSeq Stranded mRNA Kit (Illumina) and were sequenced using NovaSeq6000 (Illumina) with paired-end 150bp reads. Fastq files were preprocessed using fastp⁴⁵ and reads were mapped onto hg19 by HISAT2.⁴⁶ Mapped reads were counted using featureCounts.⁴⁷ Reads were normalized to transcripts per million (TPM). Expression fold changes were calculated using DESeq2. GSEA was performed with "GENEset" permutation, and all other parameters were set to default.⁴⁸ Expressed protein-coding genes were used.

2.8 | Real-time quantitative PCR

cDNA was synthesized using ImPromII Reverse Transcriptase (Promega). Quantitative PCR was performed on the StepOnePlus real-time PCR system (Applied Biosystems) using the FastStart Universal SYBR Green Master (Roche). Gene expression levels were evaluated using the Δ Ct method and normalized to that of *ACTB*. The primer sequences are shown in Table S1.

2.9 | ATAC-seq analysis

We analyzed our previous IPMNinv2 and PDAC1 organoid ATAC sequence data deposited in E-GEAD-416.¹² Log2CPM (count per million) scores from merged peak sets (194,222) were used. To define promoter accessibility scores shown in Figure 2B, we averaged the ATAC scores of peaks within promoter regions ($TSS \pm 5$ kb). For TF footprint analyses in Figure 2C, ATAC peaks were classified based on their compartments (higher Calder score in IPMNinv2 or PDAC1). Classified peaks and bam files were used as input for HmM-based Identification of Transcription factor footprints (HINT) analysis.⁴⁹

2.10 | ChIP-seq

Chromatin immunoprecipitation experiments were performed as described previously.¹² Briefly, cells were cross-linked using 1%

formaldehyde for 10 minutes and quenched using 125 mM glycine. Cross-linked cells were lysed and washed. Nuclear pellets were suspended in sonication buffer and sheared with a sonicator (Bioruptor UCD-250, Cosmo Bio) for 15 cycles at high output (30 seconds sonication followed by 30 seconds rest). Cleared lysates were aliquoted and stored at -80°C . Upon use, these lysates were diluted with ChIP dilution buffer and incubated with magnetic beads (Dynabeads M-280 sheep anti-rabbit IgG, Life Technologies) bound with antibodies listed in Table S2 overnight at 4°C. DNA-bound beads were washed once with low salt buffer, once with high salt buffer, and five times with LiCl buffer. Input and ChIPed DNA were eluted in elution buffer, followed by de-cross-linking overnight at 65°C. After RNase treatment and proteinase K digestion, DNA was extracted using the MinElute PCR purification kit (Qiagen). Sequencing libraries were prepared using the SMARTer ThruPLEX Tag-seq 6S Kit (Takara) and were sequenced using NextSeq500 (Illumina) with single-end 75 bp reads. Fastq files were mapped onto the hg19 using bowtie.⁵⁰ Duplicates were removed using Picard MarkDuplicates.

To focus on the HNF1B induced modification in HNF1B and H3K27ac ChIP-seq, signals over previous HNF1B ChIP-seq peaks (GSE64560)⁹ were visualized using deepTools as shown in Figures 2E and 3E.⁵¹ Likewise, in Figure 3F, HNF1B and H3K27ac reads at HNF1B peaks were extracted using featureCounts. These counts were normalized by edgeR giving log2 fold change of HNF1B and H3K27ac signals in HNF1B-overexpressed cells over empty control. For CTCF ChIP-seq, peaks against input control were called using MACS2 with a parameter $-q$ 0.01. Reads for each peak were extracted using featureCounts. Input counts were extracted from CTCF ChIP counts with negative values being set to zero. These counts were normalized by edgeR giving log2CPM. Fold enrichment signal against input was calculated using `bdgcmp` command in MACS2⁵² to create a bedgraph file followed by conversion into a bigwig file using `bedGraphToBigwig` command. The bigwig file was further adjusted using the scaling factor obtained from edgeR TMM normalization.

2.11 | Statistical analysis

The differences between experimental groups were evaluated using the two-sided Student's *t* test, Fisher's exact test, or one-way ANOVA and were considered significant at $p < 0.05$. Graphs and figures were prepared using either R package or Graph Pad Prism 9. Data are presented as Tukey's boxplot or mean \pm SEM.

3 | RESULTS

3.1 | Hi-C analysis of patient-derived organoids revealed the importance of 3D genome structure in PCs

We previously revealed that PDAC and IPMNinv, which are PCs that emerged from different precursors, PanIN and IPMN, respectively, had different open-chromatin profiles with characteristic biological

features using patient-derived organoids.¹² In this study, we attempted to address the importance of 3D genome structures in PCs using these organoids (Figure 1A). Our Hi-C data from organoids, including PDAC, IPMN, and IPMNiv, were compared with publicly available Hi-C datasets from normal pancreas,⁵³ human pancreatic nestin-expressing cells (HPNE), and PDAC cell lines (Panc-1 and Capan-1) (Figure 1B).⁵⁴ Given the possible biases of Hi-C data due to differences in preparation protocols or sequencing depth, we used the HiCRep algorithm, which is relatively robust to these biases.³⁴ We found that 3D genome profiles from Hi-C data successfully reflected the pathological differences among normal, IPMN-related lineages, and PDACs (Figure 1B). Moreover, the HPNE cell line, which mimics acinar-to-ductal metaplasia,⁵⁵ a presumable trans-differentiation step to PanIN, was classified similarly to the other PDAC cells. Next, we investigated the relationships between gene expression profiles and 3D genome modules, including compartment, TAD, and E-P loop. The depth of our Hi-C data (>2.4 billion reads) was sufficient for annotating each module.²¹ To exclude the possible effects of CNVs, RNA values were adjusted based on CNV status from previously performed exome sequencing.¹² When analyzing compartments, the importance of continuous quantification rather than canonical dichotomous classification of A and B compartments has been proposed recently.^{15,56} Therefore, we used the Calder algorithm to infer subcompartments and quantify their activities (Figure 1C).³⁵ As expected, the Calder score dictated the differences in gene expression between PDAC1 and IPMNiv2 cells (Figure 1D). Representatively, the activity of compartments was linked to the expression of *CYP2C* family genes located in the vicinity (Figure 1E). To assess the role of TAD, we used the domain score, which is defined by the ratio of intra-TAD interactions to all cis interactions and correlates well with the expression of intra-TAD genes (Figure 1F).^{17,57} Higher domain scores indicated higher gene expression between PDAC1 and IPMNiv2, as shown by the *SLC1A1* locus (Figure 1G,H). Regarding the role of the loop, we called significant loops and extracted those whose anchors matched enhancers and promoters (E-P loops) using the HiCCUPS algorithm (Figure 1I).³³ E-P loops were positively related to gene expression, as shown by the *GATA6* locus, a master PG subtype gene (Figure 1J,K; Figure S1).^{5,7} Collectively, the Hi-C data indicated that various 3D genome modules play roles in the distinct gene expression of the respective PCs.

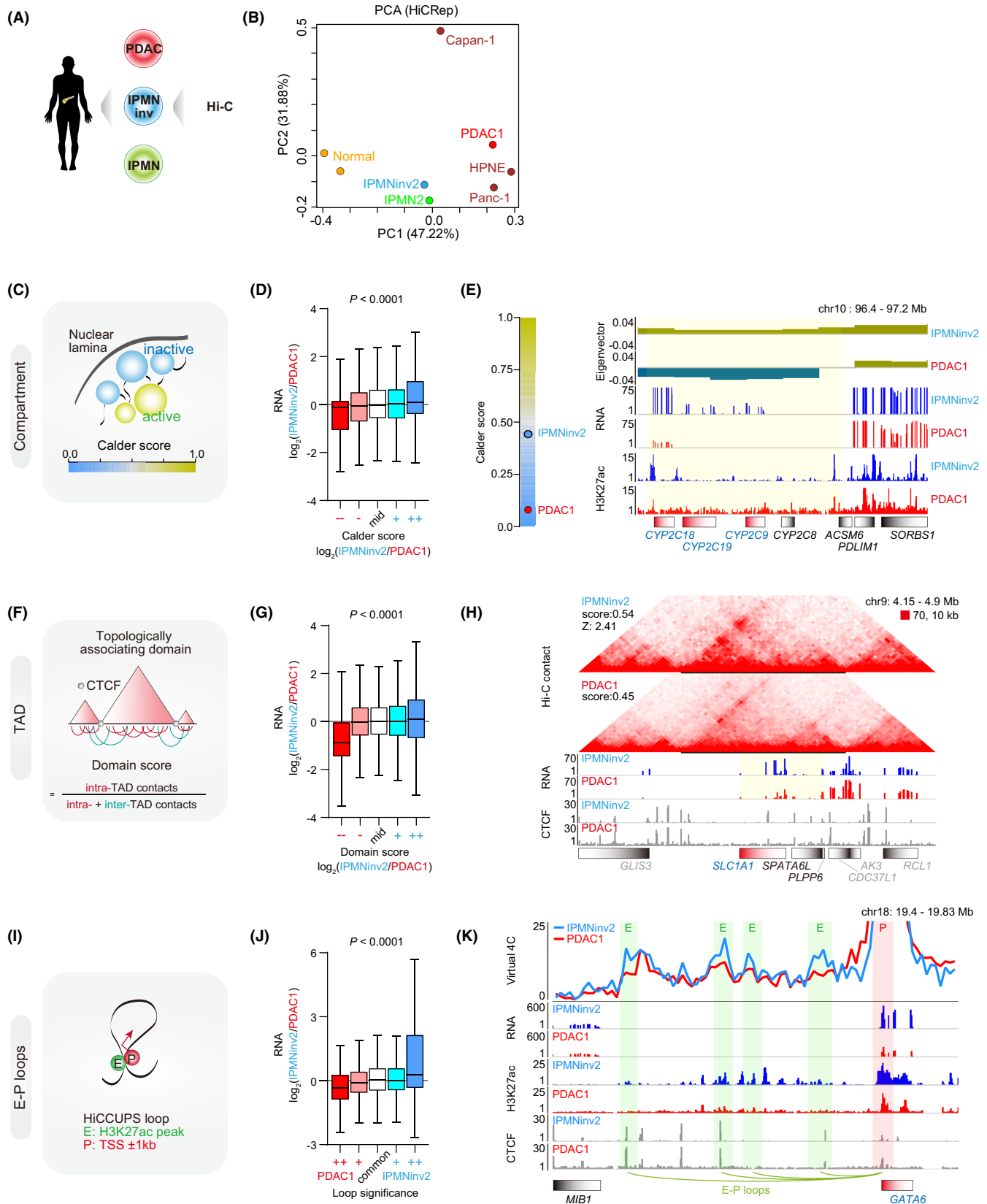
3.2 | Orchestration of multi-layer 3D genome structures underlies PG-subtype molecular signature

Among the two major transcriptional subtypes in PC, IPMNiv is often classified as the PG subtype, but not as the SQ subtype.^{3,12} Consistently, 334 genes among the previously curated 500 PG-related genes⁸ were more highly enriched in our IPMNiv organoid (IPMNiv2) than those in the SQ-subtype PDAC organoid (PDAC1) (Figure 2A). Therefore, we investigated how the 3D genome modules contribute to the molecular profiles of IPMNiv2 confined to the PG subtype. We compared the status of the 3D modules in 334

gene loci between IPMNiv2 and PDAC1 (Figure 2B). We also calculated promoter accessibility (ATAC signals within ± 5 kb of the TSS) for the local chromatin profile and CNV for reference. The compartments reflected the most remarkable score changes in 158 PG-specific genes (*CYP2C18*, *CFTR*, and *FGFR4*) (47.3%) among the 3D modules (Figure 2B). The Calder score of the compartments showed the highest correlation with the expression of 334 PG-specific genes (Figure S2A). In addition, compartment activity was significantly related to a higher domain score, E-P interaction, and promoter accessibility (Figure S2B), which corroborates the notion that compartments concentrate functionally related molecules and govern gene regulation.⁵⁸ The increase in E-P loop interaction underpinned 28 key PG-specific genes (8.4%), including *GATA6*, *BMP4*,⁵⁹ and *SHH*⁶⁰ in IPMNiv2 (Figure 2B), which is consistent with the previous finding that cell type-specific genes are connected to enhancer elements and fine-tuned by E-P loops.⁶¹ The promoter accessibility had a positive relation to 49 PG-specific genes (14.7%), including *HNF4A* and *PDX1*, which supports the previous findings that those promoters are being inactivated by methylation in the SQ subtype.³ In contrast, the contribution of CNVs was very limited (correlation coefficient (r) = 0.03) (Figure S2A). Having demonstrated the potency of these compartments in the expression of PG-specific genes, we focused on the factors that regulate their activity. Recently, the involvement of TF-induced phase separation has been proposed as a driving force for establishing compartments.²⁷⁻³¹ At first, we aimed to identify the TFs that may have a role in the active compartments of PG-specific genes in IPMNiv2. In a previous report, we identified HNF1B as one of the highly enriched TFs in IPMNiv, but not in PDAC, using TF footprint analysis in ATAC-seq.¹² We further investigated whether this HNF1B enrichment is related to the activity of compartments. We subdivided the genome of IPMNiv2 based on compartment activity compared with PDAC1: either more active in IPMNiv2 or less active in IPMNiv2. The enrichment of HNF1B was found in compartments that were more active in IPMNiv2 (Figure 2C). Moreover, traditional compartment analysis classifying the genome into active A or inactive B compartments also showed a greater enrichment of HNF1B binding sites in compartment A of IPMNiv2 (Figure S2C). Hence, we speculated that HNF1B might play a role in the more active PG-specific compartments observed in IPMNiv2.

3.3 | HNF1B contributes to the expression of PG-subtype genes and modulates the underlying 3D genomic structure

To test this hypothesis, we overexpressed HNF1B (HNF1B^{OE}) in PDAC1 cells (Figure 2D). ChIP-seq validated the enrichment of HNF1B bindings in its known target elements (Figure 2E). HNF1B^{OE} recapitulated the expression of 334 IPMNiv2-enriched PG genes (Figure 2F). In addition, 313 HNF1B^{OE}-induced PG-specific genes were more enriched in IPMNiv2 than those in PDAC1 (Figure S2D). We then performed Hi-C to unveil the HNF1B-induced 3D genome



modulation. As the replicates showed good reproducibility, we combined them for all subsequent analyses (Figure S2E). Among the 3D modules, the increased activity of the compartment

reflected the expression of 144 PG-specific genes, such as the CYP2C family genes, after HNF1B OE (Figure S2F). Moreover, the Calder score changes of the 334 PG genes in HNF1B^{OE} PDAC1

FIGURE 1 3D genome architecture associates with gene expression in pancreatic cancer organoids. A, Scheme of patient-derived organoids used for Hi-C experiments. B, Principal component analysis (PCA) of organoids combined with reported pancreas Hi-C dataset uncovering the overall trend in pancreas neoplasms. C-E, Scheme of analyzing compartments using Calder compartment score (C), relation of compartment activity to RNA expression (D), and example of differential compartment as seen in *CYP2C* family gene locus (E). Tracks of Hi-C eigenvector value (100kb resolution), RNA, and H3K27ac are also shown. Compartment of interest is highlighted. F-H, Scheme of analyzing topologically associating domains (TADs) using domain score (F), relation of TAD activity to RNA expression (G), and example of differential TADs as seen in *SLC1A1* locus with RNA and CCCTC-binding factor (CTCF) tracks (H). The black bars denote TAD of interest. Domain scores and a Z-score are also shown. Expression of genes whose promoters are encompassed within this TAD are highlighted. Contacts are shown at a 10kb resolution. I-K, Scheme of analyzing enhancer-promoter (E-P) loops called by HiCCUPS (I), relation of E-P loop significance to RNA expression (J), and example of differential E-P loops as seen in *GATA6* locus with tracks of virtual 4C (5 kb resolution), RNA, H3K27ac, and CTCF (K). The enhancers and promoter are highlighted in green and red, respectively. The loops called only in IPMNinv2 are shown. Z-scores from log₂ fold change of Calder score and domain score were used to classify them ($Z < -1.96$, --; $-1.96 < Z < -0.5$, -; $-0.5 < Z < 0.5$, mid; $0.5 < Z < 1.96$, +; $1.96 < Z$, ++). E-P loops were classified according to their significance (loops called by HiCCUPSDiff, -- or ++; loops called by HiCCUPS, - and +; loops called in both samples, common). For box plots, center lines represent medians; box limits represent 25% and 75% quantiles; whiskers represent the smallest or largest observation within 1.5× of the interquartile range. *P* values were determined using one-way ANOVA. Genes are denoted by boxes with their transcription start site (TSS) sides colored densely

cells correlated well with the score differences between IPMNinv2 and PDAC1 ($r = 0.28$, $P = 1.6 \times 10^{-7}$), suggesting that the different compartment profiles between IPMNinv2 and PDAC1 could be partially directed by HNF1B (Figure 2G). Increased E-P interactions underpinned 34 PG-specific genes, including *GATA6* and *BMP4*, which were differentially expressed in IPMNinv2 and PDAC1 (Figure S2F). These results highlight the importance of HNF1B-induced chromatin structures in the differential expression profiles of IPMNinv2 and PDAC1.

3.4 | HNF1B^{OE} facilitated long-range genomic interactions and compartment activation

Transcriptional factors often establish long-range genomic interactions via condensation to regulate cell-specific gene expression.^{17,43,62} Thus, we examined the distribution of HNF1B within the nucleus by immunofluorescence analysis. Immunofluorescence images of HNF1B showed several concentrated nuclear foci distributed away from the Hoechst signal, which delineates tightly packed heterochromatin (Figure 3A),⁶³ suggesting that HNF1B assembled in the open-chromatin-rich active compartment. To further visualize the relationship between the active compartment and long-range genomic crosstalk after HNF1B^{OE}, we analyzed the genome-wide interactions among HNF1B binding sites using paired-end spatial chromatin (PE-SCAn) analysis.⁴³ The long-range genomic interactions among HNF1B binding sites were increased in the activated compartments (defined as the increased Calder score by HNF1B^{OE}), but not in the inactivated compartments (defined as the decreased Calder score by HNF1B^{OE}) (Figure 3B; Figure S3A), suggesting the possibility that HNF1B condensation synchronized with compartment activation. Moreover, we found newly established interactions of HNF1B binding sites between compartments activated from the Calder-low (Calder score: 0-0.5) and Calder-high (Calder score: 0.5-1) compartments (Figure 3C,D). Compartment strength analysis, which computes the interactions between the active A and inactive

B compartments, showed that HNF1B^{OE} induced intercompartment interactions (Figure S3B). These results indicated that HNF1B^{OE} facilitates long-range genomic interactions accompanied by compartment activation (Figure 3D).

3.5 | HNF1B^{OE}-induced compartment modulation is associated with H3K27ac redistribution and altered expression of subtype-related genes

Next, we investigated how HNF1B^{OE}-induced compartment modulation is supported by other chromatin profiles and the extent to which it is related to gene expression. Generally, the activity of TFs cooperates with H3K27ac status or transcriptional coactivators, such as histone-acetyltransferases.⁶⁴ H3K27ac dynamics have recently been found to modulate the interaction frequency between regulatory regions.⁵⁶ Therefore, we examined the H3K27ac profiles induced by HNF1B^{OE}. Although global H3K27ac levels were not influenced by HNF1B^{OE} (Figure 2D), H3K27ac signals and HNF1B binding were preferentially increased in the activated compartments compared with those in the inactivated compartments genome-wide (Figure 3E), which was consistent with the enriched distribution of HNF1B targets within the activated compartments (Figure 3B; Figure S3C). In addition, when we focused on the PG gene-related compartments, HNF1B signals, H3K27ac modification, and RNA levels were significantly increased in the activated compartments (Figure S3D). More importantly, these values were significantly correlated in the activated compartments ($r = 0.30$, 0.34 , and 0.39 , respectively) but not in the inactivated compartments (Figure 3F; Figure S3E). Representatively, the *CYP2C* family gene locus showed compartment activation in relation to the increase in HNF1B and H3K27ac signals of their regulatory elements with their corresponding gene expression (Figure 3G,H). These results suggest a possible cooperation between compartment activation and H3K27ac modification of the HNF1B-directed expression of PG-related genes.

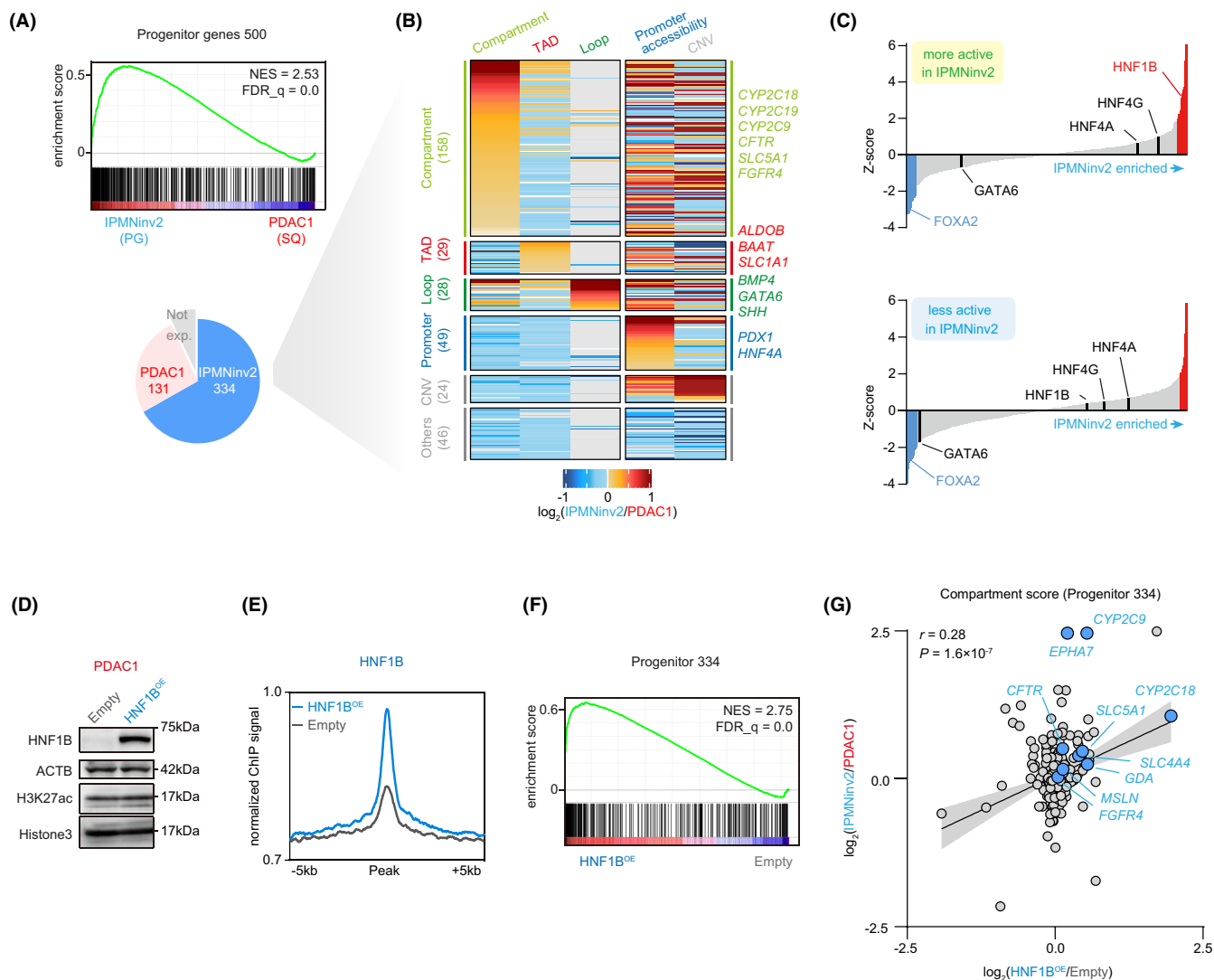


FIGURE 2 Orchestration of multilayer 3D genome structures underlies progenitor (PG)-subtype molecular signature. A, Gene set enrichment analysis (GSEA) result of 500 PG genes between IPMNinv2 (PG) and PDAC1 (squamous [SQ]). 334 genes out of them were highly expressed in IPMNinv2. B, Heatmap of \log_2 fold change scores of each 3D genome module related to 334 PG genes between IPMNinv2 and PDAC1. Each gene was assigned to the highest scoring modules among compartments, TADs, and enhancer-promoter (E-P) loops. Promoter activities and copy number variations (CNVs) are shown for reference and used for assignment when gene expression could not be explained by any of the 3D genome modules. C, ATAC-seq footprint analysis showing the enrichment profile of TFs in IPMNinv2, classified by compartments that have higher Calder score in IPMNinv2 (top, more active in IPMNinv2) or in PDAC1 (bottom, less active in IPMNinv2). Note that among known PG transcriptional factors (TFs) that are highlighted, enrichment of HNF1B was evident in the more active compartments in IPMNinv2, but not in the less active compartments in IPMNinv2. Significant TFs are colored either red ($Z > 1.96$) or blue ($Z < -1.96$). D, Western blot showing induction of HNF1B in PDAC1 with least effect on global H3K27ac amount. E, HNF1B chromatin immunoprecipitation sequencing (ChIP-seq) profile over HNF1B peaks showing its effective enrichment in HNF1B^{OE}. F, GSEA result showing effective induction of 334 PG genes in HNF1B^{OE}. G, Scatter plot of \log_2 fold change compartment scores between HNF1B^{OE}/empty and IPMNinv2/PDAC1. Compartments related to representative genes are shown

3.6 | HNF1B-mediated 3D modules accompanied with reciprocal changes in subtype-related gene expression

While we focused on the role of HNF1B in PG-subtype gene regulation, we also observed the downregulation of some SQ genes (254 out of 500 genes), leading to subtype switching after HNF1B^{OE}

(Figure S3F,G). In addition, the altered status of the 3D modules was synchronized with the suppression of these SQ genes (Figure 3I). Compartments and TADs reflected 93 (36.6%) and 88 (34.6%) SQ genes, respectively, including *COL6A*, *LOX*, and *KRT* family genes, and epithelial mesenchymal transition markers (*SNAI2*, *TGFBI*, *ALDH1A3*, and *SIX4*) (Figure 3I). Twenty-seven (10.6%) SQ genes, including *TGF2*, were underpinned by E-P loops (Figure 3I). To clarify the landscape of

compartment modulation in the reciprocal changes in subtype-related gene expression, we visualized the Calder score changes of both up-regulated PG and downregulated SQ genes after HNF1B^{OE} (Figure 3J). The analysis showed that PG genes in Calder-low compartments, such as *CYP2C* family genes, were significantly activated, and SQ genes in Calder-high compartments, such as *SNAI2*, *ALDH1A3*, and *TGFBI*, were significantly inactivated after HNF1B^{OE} in PDAC1 (Figure 3J). These data imply critical cooperation between HNF1B-driven 3D structural modification and reciprocal regulation of subtype-specific genes.

3.7 | HNF1B^{OE}-induced reciprocal changes in subtype-related genes required the IDR of HNF1B

Recently, the IDR was reported to drive transcriptional phase-separated condensates because of their low amino acid sequence complexity, typically enriched in polar and charged amino acids, including glycine, serine, glutamine, asparagine, phenylalanine, and tyrosine.^{27,65-67} When we searched for the IDR of HNF1B by its amino acid arrangements (Figure 4A), HNF1B embraced a structureless disordered region of 321-466 amino acids, which was enriched with serine, establishing an IDR (Figure S4A). This region matches with the previously known transactivation domain, which synergistically acts with histone acetyltransferases.⁶⁸ Mutations in this HNF1B IDR are related to various diseases.^{64,68} Therefore, we induced mutant HNF1B, whose IDR was either deleted (HNF1B-dIDR) or substituted by an IDR from another peptide AKAP95 (HNF1B-AKAP95), whose amino acid position 101-210 is well studied to form transcriptional phase-separated condensates (Figure 4A,B; Figure S4A).^{30,69} While wild-type HNF1B upregulated PG genes and downregulated SQ genes that were supported by compartments and E-P loops (Figures 2B and 3H), these effects were diminished by HNF1B-dIDR or recapitulated by HNF1B-AKAP95, suggesting the functional importance of IDRs (Figure 4C). These trends were also observed in another SQ-type PC cell line, BxPC-3 (Figure S4B). Additionally, HNF1B and HNF1B-AKAP95 induction in this cell line induced morphological changes to form duct-like colonies, which were canceled in HNF1B-dIDR (Figure S4C). Collectively, these data suggest the possible involvement of IDR-driven mechanisms in HNF1B^{OE}-induced transcriptional alterations.

4 | DISCUSSION

The molecular subtype of PC is currently a major topic of research because of its direct association with patient outcomes. PG subtypes are associated with a better prognosis, whereas SQ subtypes tend to be associated with more aggressive, metastatic, and chemotherapy-resistant phenotypes. Many reports have aimed to unveil the mechanism behind these differences by focusing on certain TFs, such as GATA6, HNF4A, and TP63.⁶⁻⁸ However, the mechanism by which

these molecular signatures of PCs are established remains unclear. In particular, while the importance of 3D genome structures in cell type-specific gene expression has become significant, attempts to uncover subtype-specific gene expression from a 3D genome perspective have been lacking in PC. Here, inspired by the fact that IPMN-derived cancers are preferentially classified as PG subtypes and that we have previously revealed the indispensability of HNF1B in IPMN lineages, together with its importance in chromatin profiles, we speculated that HNF1B may contribute to maintaining PG subtypes in PCs through 3D chromatin structures.

Although Hi-C has been applied to some PC cell lines,⁵⁴ there have been no reports examining the genomic structure of PC in patient samples. Here, we visualized how the 3D genomic structure changed following HNF1B induction using PC-derived organoids. However, the number of Hi-C-analyzed samples was limited. Future studies using larger sample sizes are warranted to test our findings and generalize the association between genome structure and transcriptional subtypes.

We observed different genomic structures in different modes of pancreatic tumorigenesis, including IPMN and PDAC. It may also be interesting to study these tumors from a 3D genomic perspective to unveil their nature. Furthermore, HNF1B is associated with many other diseases, including diabetes mellitus.⁶⁸ We hope that our mapping of HNF1B-induced 3D genome remodeling will be useful for studying these diseases.

Although we focused on HNF1B, a number of epigenetic molecules, including other TFs, mediators, cofactors, noncoding RNAs, or histone modifiers, should coordinately play important roles in genomic structures.⁵⁸ It may be helpful to evaluate the physical interaction or colocalization of HNF1B with other molecules, for example, histone acetyltransferases such as p300, to further clarify the mechanism of HNF1B-associated H3K27ac redistribution or compartment activation. In addition, we did not assess the involvement of HNF1A, a paralog of HNF1B that binds to the same consensus sequence on DNA.⁶⁸ Therefore, it remains to be elucidated whether HNF1A plays any role in the phenotype switch of PCs.

Our data imply the possible involvement of TF-induced phase separation in transcriptional remodeling, which is now attracting attention as a therapeutic target⁷⁰ for its potential to concentrate cancer drugs²⁹ or to be selectively targeted.⁷¹ Our experiments showed the importance of IDRs in regulating subtype-specific genes. However, because the HNF1B-dIDR mutant lacks most of the transactivation domain, the data may not fully distinguish the impact of this IDR deletion from canonical activities, such as recruitment of cofactors, including histone acetyltransferases. We admit that additional insights, such as the kinetics of a liquid droplet (which could be measured by dose-dependent condensation or photo-bleach interrogation) or direct visualization of droplet-driven genome modulation (eg, 3D-FISH, live-cell time-lapse imaging) are required to fully provide definitive proof of phase separation as a next step.

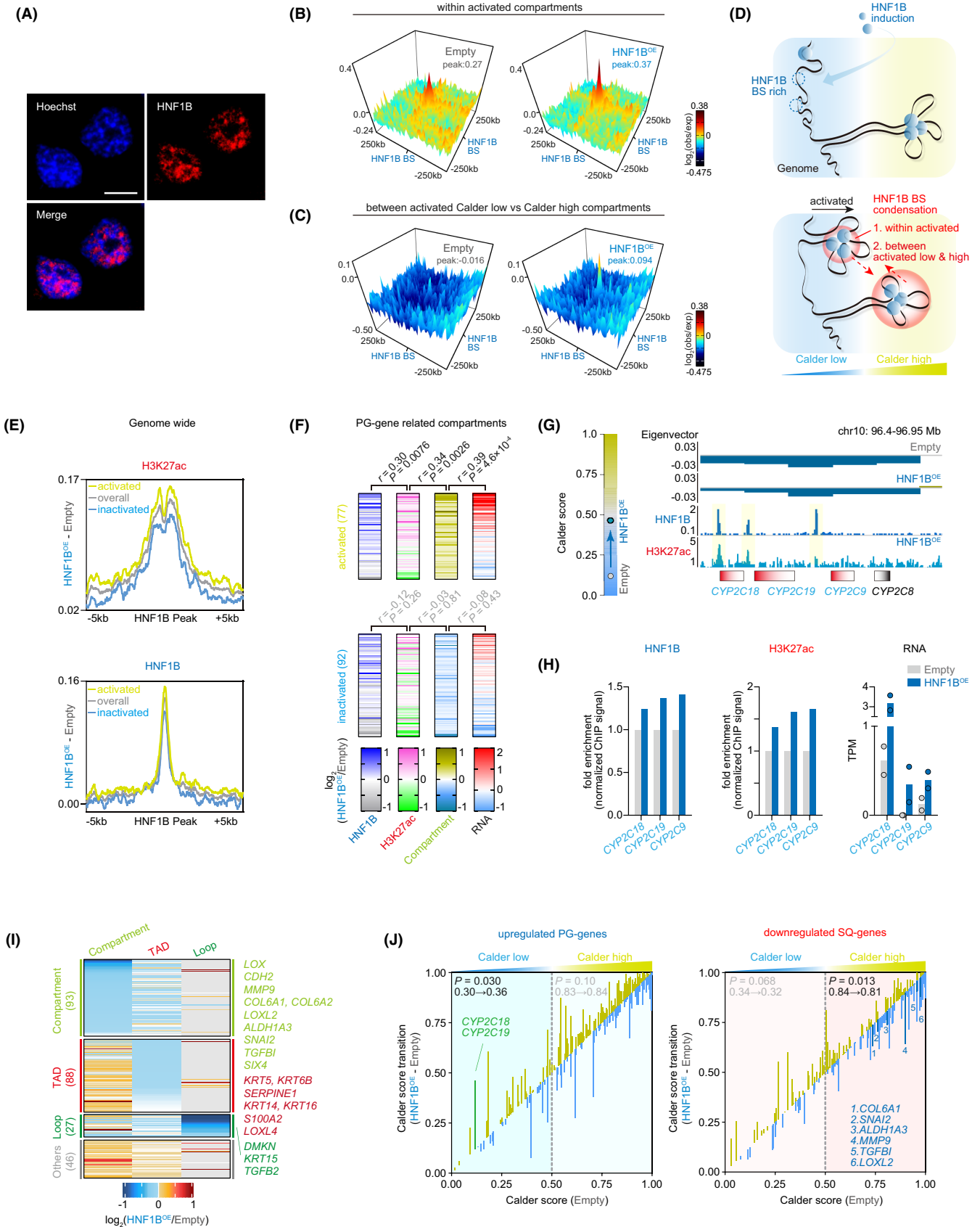


FIGURE 3 HNF1B^{OE}-induced long-range genomic interaction is associated with compartment modulation, H3K27ac redistribution, and altered expression of subtype-related genes. **A**, Immunofluorescent image in HNF1B^{OE} cells. HNF1B signals are concentrated at nuclear foci preferentially distributed away from Hoechst signal. Scale bar, 10 μ m. **B, C**, Metaplots of interactions among HNF1B binding sites. This visualization depicts interactions of pairs of HNF1B binding sites that are >5 Mb apart at 10kb resolution. The interaction intensity (log₂(observed/expected)) is shown on the z axis and by the color scale. Area is centered on the HNF1B binding sites with 250 kb upstream and downstream loci. **B**, Interactions among HNF1B binding sites within compartments that are activated after HNF1B^{OE} (N = 1490). **C**, Interactions between HNF1B binding sites that were activated from Calder-low compartments (N = 486) and those within Calder high compartments (N = 1853). Scores at the HNF1B binding center (denoted as peak) are also shown. BS, binding site. **D**, Scheme of compartment modulation in HNF1B^{OE} representing that HNF1B binding site condensation (denoted as red area) is seen within activated compartments and between activated Calder-low and -high compartments; this suggests that compartment activation is accompanied by HNF1B-induced long-range genomic interactions. **E**, HNF1B and H3K27ac chromatin immunoprecipitation sequencing (ChIP-seq) profile over HNF1B peaks. Signals are shown as (HNF1B^{OE} - Empty) within subclassified compartments (activated, inactivated, or overall compartments). **F**, Log₂ fold change of HNF1B, H3K27ac, Calder score, and RNA expression within PG gene-related compartments after HNF1B^{OE}. Average of all HNF1B signals, H3K27ac signals, and gene expressions encompassed by each compartment are shown. Z-scores of log₂ fold change Calder score were used to classify compartments (Z < -0.3, inactivated; 0.3 < Z, activated). **G**, Representative locus of HNF1B-induced compartment activation (CYP2C family gene locus). Calder score and Hi-C eigenvector value are shown to represent compartment activity together with HNF1B (GSE64560) and H3K27ac tracks. **H**, Signals of HNF1B and H3K27ac ChIP-seq at regulatory elements of respective CYP2C family genes highlighted in (G), and their RNA expression. **I**, Heatmap of log₂ fold change scores of each 3D genome module related to downregulated squamous (SQ) genes (254) in HNF1B^{OE}. **J**, Transition of compartment scores of upregulated progenitor (PG) and downregulated SQ genes in HNF1B^{OE}. Genes are sorted based on their Calder scores in empty samples (x axis). Calder score transitions are denoted in the y axis and colored yellow (activation) or blue (inactivation). P values were determined by two-sided paired t test. Median score changes are also shown

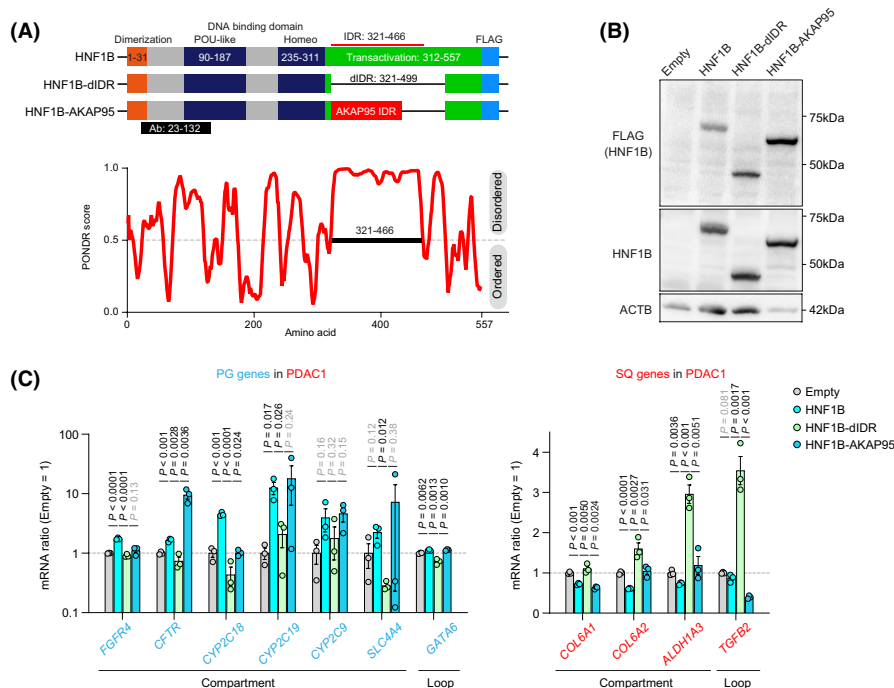


FIGURE 4 HNF1B^{OE}-induced reciprocal changes in subtype-related genes required intrinsically disordered region (IDR) of HNF1B. **A**, (Top) Protein structures of HNF1B and their mutants with functional annotation designated by amino acid positions. Ab, antibody recognition site. (Bottom) Plotting of intrinsic disorder in HNF1B. Predictor of Natural Disordered Regions (PONDR) scores are shown on the y axis, and amino acid positions are shown on the x axis. The black bar represents the predicted IDR. **B**, Western blot showing expression of HNF1B and its mutants presenting their expected size. **C**, mRNA expression (qPCR) of representative progenitor (PG) and squamous (SQ) genes after induction of HNF1B and its mutants (n = 3, biological replicates). Expressions were internally normalized by ACTB and empty control. Data are shown as the mean \pm SEM. P values were determined by two-sided unpaired t test

Our perspective on TF-induced 3D chromatin remodeling may open a new era in PC research. We propose that TFs may act as directional rudders to change the higher-order structure of chromatin and determine PC subtype.

ACKNOWLEDGMENTS

This study was supported by grants from the Japan Society for the Promotion of Science Kakenhi (Grant Number 16H06279 (PAGS), 19K08435, 21K15966, 21K20828, 22H02898, 22H03053),

Uehara Memorial Foundation, Takeda Science Foundation, Yasuda Medical Foundation, Tokyo Society of Medical Sciences, MSD Life Science Foundation, Astellas Foundation for Research on Metabolic Disorders, Princess Takamatsu Cancer Research Fund, Life Science Foundation of Japan, and International Joint Usage/Research Center, Institute of Medical Science, University of Tokyo. We thank Sayaka Ito for technical assistance and all lab members for their helpful comments.

DATA AVAILABILITY STATEMENT

Raw human sequencing data have been uploaded to the Japanese Genotype-phenotype Archive (JGA) under accession no. JGAS000514, and processed data are deposited in the Gene Expression Omnibus (GEO) with accession no. GSE202023. Previous sequencing data for organoids used in this study are found with accession numbers as follows: JGAS000262 (Hi-C), JGAS000263 (whole exome-seq and RNA-seq), and JGAS000264 (ATAC-seq and ChIP-seq).

ETHICS STATEMENT

- Approval of the research protocol by an Institutional Reviewer Board. This study was approved by the ethical committee of the University of Tokyo Hospital.

- Informed Consent. Written informed consent was obtained from all patients.

- Registry and the Registration No. of the study/trial. "N/A."

- Animal Studies. "N/A."

DISCLOSURE

The authors declare no conflict of interest.

ORCID

Hiroyuki Kato  <https://orcid.org/0000-0003-0655-1519>

Keisuke Tateishi  <https://orcid.org/0000-0002-9837-0856>

Keisuke Yamamoto  <https://orcid.org/0000-0002-6323-9540>

Yotaro Kudo  <https://orcid.org/0000-0003-1869-2810>

Yoku Hayakawa  <https://orcid.org/0000-0002-3988-2499>

REFERENCES

- Collisson EA, Sadanandam A, Olson P, et al. Subtypes of pancreatic ductal adenocarcinoma and their differing responses to therapy. *Nat Med*. 2011;17(4):500-503. doi:10.1038/nm.2344
- Moffitt RA, Marayati R, Flate EL, et al. Virtual microdissection identifies distinct tumor- and stroma-specific subtypes of pancreatic ductal adenocarcinoma. *Nat Genet*. 2015;47(10):1168-1178. doi:10.1038/ng.3398
- Bailey P, Chang DK, Nones K, et al. Genomic analyses identify molecular subtypes of pancreatic cancer. *Nature*. 2016;531(7592):47-52. doi:10.1038/nature16965
- Chan-Seng-Yue M, Kim JC, Wilson GW, et al. Transcription phenotypes of pancreatic cancer are driven by genomic events during tumor evolution. *Nat Genet*. 2020;52(2):231-240. doi:10.1038/s41588-019-0566-9
- O'Kane GM, Grunwald BT, Jang GH, et al. GATA6 expression distinguishes classical and basal-like subtypes in advanced pancreatic cancer. *Clin Cancer Res*. 2020;26(18):4901-4910. doi:10.1158/1078-0432.CCR-19-3724
- Camolotto SA, Belova VK, Torre-Healy L, et al. Reciprocal regulation of pancreatic ductal adenocarcinoma growth and molecular subtype by HNF4 α and SIX1/4. *Gut*. 2021;70(5):900-914. doi:10.1136/gutjnl-2020-321316
- Kloesch B, Ionasz V, Paliwal S, et al. A GATA6-centred gene regulatory network involving HNFs and Δ np63 controls plasticity and immune escape in pancreatic cancer. *Gut*. 2022;71(4):766-777. doi:10.1136/gutjnl-2020-321397
- Somerville TDD, Xu Y, Miyabayashi K, et al. TP63-mediated enhancer reprogramming drives the squamous subtype of pancreatic ductal adenocarcinoma. *Cell Rep*. 2018;25(7):1741-1755.e7. doi:10.1016/j.celrep.2018.10.051
- Diaferia GR, Balestrieri C, Prosperini E, et al. Dissection of transcriptional and cis-regulatory control of differentiation in human pancreatic cancer. *EMBO J*. 2016;35(6):595-617. doi:10.15252/embj.201592404
- Hruban RH, Adsay NV, Albores-Saavedra J, et al. Pancreatic intraepithelial neoplasia. *Am J Surg Pathol*. 2001;25(5):579-586. doi:10.1097/0000478-200105000-00003
- Furukawa T, Klöppel G, Volkan Adsay N, et al. Classification of types of intraductal papillary-mucinous neoplasm of the pancreas: a consensus study. *Virchows Arch*. 2005;447(5):794-799. doi:10.1007/s00428-005-0039-7
- Kato H, Tateishi K, Fujiwara H, et al. MNX1-HNF1B Axis is indispensable for intraductal papillary mucinous neoplasm lineages. *Gastroenterology*. 2022;162(4):1272-1287.e16. doi:10.1053/j.gastro.2021.12.254
- Kloetgen A, Thandapani P, Ntziachristos P, et al. Three-dimensional chromatin landscapes in T cell acute lymphoblastic leukemia. *Nat Genet*. 2020;52(4):388-400. doi:10.1038/s41588-020-0602-9
- Beagan JA, Phillips-Cremens JE. On the existence and functionality of topologically associating domains. *Nat Genet*. 2020;52(1):8-16. doi:10.1038/s41588-019-0561-1
- Johnstone SE, Reyes A, Qi Y, et al. Large-scale topological changes restrain malignant progression in colorectal cancer. *Cell*. 2020;182(6):1474-1489.e23. doi:10.1016/j.cell.2020.07.030
- Zheng H, Xie W. The role of 3D genome organization in development and cell differentiation. *Nat Rev Mol Cell Biol*. 2019;20(9):535-550. doi:10.1038/s41580-019-0132-4
- Stadhouders R, Vidal E, Serra F, et al. Transcription factors orchestrate dynamic interplay between genome topology and gene regulation during cell reprogramming. *Nat Genet*. 2018;50(2):238-249. doi:10.1038/s41588-017-0030-7
- Okabe A, Huang KK, Matsusaka K, et al. Cross-species chromatin interactions drive transcriptional rewiring in Epstein-Barr virus-positive gastric adenocarcinoma. *Nat Genet*. 2020;52(9):919-930. doi:10.1038/s41588-020-0665-7
- Lieberman-Aiden E, van Berkum NL, Williams L, et al. Comprehensive mapping of long-range interactions reveals folding principles of the human genome. *Science*. 2009;326(5950):289-293. doi:10.1126/science.1181369
- Dixon JR, Selvaraj S, Yue F, et al. Topological domains in mammalian genomes identified by analysis of chromatin interactions. *Nature*. 2012;485(7398):376-380. doi:10.1038/nature11082
- Rao SSP, Huntley MH, Durand NC, et al. A 3D map of the human genome at kilobase resolution reveals principles of chromatin looping. *Cell*. 2014;159(7):1665-1680. doi:10.1016/j.cell.2014.11.021
- Hnisz D, Day DS, Young RA. Insulated neighborhoods: structural and functional units of mammalian gene control. *Cell*. 2016;167(5):1188-1200. doi:10.1016/j.cell.2016.10.024
- Nuebler J, Fudenberg G, Imakaev M, Abdennur N, Mirny LA. Chromatin organization by an interplay of loop extrusion and

- compartmental segregation. *Proc Natl Acad Sci USA*. 2018;115(29):E6697-E6706. doi:10.1073/pnas.1717730115
24. Rao SSP, Huang SC, Glenn St Hilaire B, et al. Cohesin loss eliminates all loop domains. *Cell*. 2017;171(2):305-320. doi:10.1016/j.cell.2017.09.026
 25. Nora EP, Goloborodko A, Valton AL, et al. Targeted degradation of CTCF decouples local insulation of chromosome domains from genomic compartmentalization. *Cell*. 2017;169(5):930-944. doi:10.1016/j.cell.2017.05.004
 26. Schwarzer W, Abdennur N, Goloborodko A, et al. Two independent modes of chromatin organization revealed by cohesin removal. *Nature*. 2017;551(7678):51-56. doi:10.1038/nature24281
 27. Boija A, Klein IA, Sabari BR, et al. Transcription factors activate genes through the phase-separation capacity of their activation domains. *Cell*. 2018;175(7):1842-1855. doi:10.1016/j.cell.2018.10.042
 28. Hildebrand EM, Dekker J. Mechanisms and functions of chromosome compartmentalization. *Trends Biochem Sci*. 2020;45(5):385-396. doi:10.1016/j.tibs.2020.01.002
 29. Klein IA, Boija A, Afeyan LK, et al. Partitioning of cancer therapeutics in nuclear condensates. *Science*. 2020;368(6497):1386-1392. doi:10.1126/science.aaz4427
 30. Shi B, Li W, Song Y, et al. UTX condensation underlies its tumour-suppressive activity. *Nature*. 2021;597(7878):726-731. doi:10.1038/s41586-021-03903-7
 31. Ahn JH, Davis ES, Daugird TA, et al. Phase separation drives aberrant chromatin looping and cancer development. *Nature*. 2021;595(7868):591-595. doi:10.1038/s41586-021-03662-5
 32. Ootani A, Li X, Sangiorgi E, et al. Sustained in vitro intestinal epithelial culture within a Wnt-dependent stem cell niche. *Nat Med*. 2009;15(6):701-706. doi:10.1038/nm.1951
 33. Durand NC, Shamim MS, Machol I, et al. Juicer provides a one-click system for analyzing loop-resolution hi-C experiments. *Cell Syst*. 2016;3(1):95-98. doi:10.1016/j.cels.2016.07.002
 34. Yang T, Zhang F, Yardimci GG, et al. HiCRep: assessing the reproducibility of hi-C data using a stratum-adjusted correlation coefficient. *Genome Res*. 2017;27(11):1939-1949. doi:10.1101/gr.220640.117
 35. Liu Y, Nanni L, Sungalee S, et al. Systematic inference and comparison of multi-scale chromatin sub-compartments connects spatial organization to cell phenotypes. *Nat Commun*. 2021;12(1):2439. doi:10.1038/s41467-021-22666-3
 36. Wolff J, Bhardwaj V, Nothjunge S, et al. Galaxy HiCExplorer: a web server for reproducible hi-C data analysis, quality control and visualization. *Nucleic Acids Res*. 2018;46(W1):W11-W16. doi:10.1093/nar/gky504
 37. Robinson MD, McCarthy DJ, Smyth GK. edgeR: a Bioconductor package for differential expression analysis of digital gene expression data. *Bioinformatics*. 2009;26(1):139-140. doi:10.1093/bioinformatics/btp616
 38. Love MI, Huber W, Anders S. Moderated estimation of fold change and dispersion for RNA-seq data with DESeq2. *Genome Biol*. 2014;15(12):550. doi:10.1186/s13059-014-0550-8
 39. Greenwald WW, Li H, Smith EN, Benaglio P, Nariai N, Frazer KA. Pgltools: a genomic arithmetic tool suite for manipulation of hi-C peak and other chromatin interaction data. *BMC Bioinformatics*. 2017;18(1):1-6. doi:10.1186/s12859-017-1621-0
 40. Sahin M, Wong W, Zhan Y, Van Deynze K, Koche R, Leslie CS. HiC-DC+ enables systematic 3D interaction calls and differential analysis for hi-C and HiChIP. *Nat Commun*. 2021;12(1):1-11. doi:10.1038/s41467-021-23749-x
 41. Durand NC, Robinson JT, Shamim MS, et al. Juicebox provides a visualization system for hi-C contact maps with unlimited zoom. *Cell Syst*. 2016;3(1):99-101. doi:10.1016/j.cels.2015.07.012
 42. Kaul A, Bhattacharyya S, Ay F. Identifying statistically significant chromatin contacts from hi-C data with FitHiC2. *Nat Protoc*. 2020;15(3):991-1012. doi:10.1038/s41596-019-0273-0
 43. de Wit E, Bouwman BAM, Zhu Y, et al. The pluripotent genome in three dimensions is shaped around pluripotency factors. *Nature*. 2013;501(7466):227-231. doi:10.1038/nature12420
 44. Van Der Weide RH, Van Den Brand T, Haarhuis JHI, Teunissen H, Rowland BD, De Wit E. Hi-C analyses with GENOVA: a case study with cohesin variants. *NAR Genomics Bioinforma*. 2021;3(2):1-15. doi:10.1093/nargab/lqab040
 45. Chen S, Zhou Y, Chen Y, Gu J. Fastp: an ultra-fast all-in-one FASTQ preprocessor. *Bioinformatics*. 2018;34(17):884-890. doi:10.1093/bioinformatics/bty560
 46. Kim D, Paggi JM, Park C, Bennett C, Salzberg SL. Graph-based genome alignment and genotyping with HISAT2 and HISAT-genotype. *Nat Biotechnol*. 2019;37:907-915. doi:10.1038/s41587-019-0201-4
 47. Liao Y, Smyth GK, Shi W. featureCounts: an efficient general purpose program for assigning sequence reads to genomic features. *Bioinformatics*. 2014;30(7):923-930. doi:10.1093/bioinformatics/btt656
 48. Subramanian A, Tamayo P, Mootha VK, et al. Gene set enrichment analysis: a knowledge-based approach for interpreting genome-wide expression profiles. *Proc Natl Acad Sci U S A*. 2005;102(43):15545-15550. doi:10.1073/pnas.0506580102
 49. Li Z, Schulz MH, Look T, Begemann M, Zenke M, Costa IG. Identification of transcription factor binding sites using ATAC-seq. *Genome Biol*. 2019;20(1):45. doi:10.1186/s13059-019-1642-2
 50. Langmead B, Trapnell C, Pop M, Salzberg SL. Ultrafast and memory-efficient alignment of short DNA sequences to the human genome. *Genome Biol*. 2009;10(3):R25. doi:10.1186/gb-2009-10-3-r25
 51. Ramírez F, Dündar F, Diehl S, Grüning BA, Manke T. DeepTools: a flexible platform for exploring deep-sequencing data. *Nucleic Acids Res*. 2014;42(W1):187-191. doi:10.1093/nar/gku365
 52. Zhang Y, Liu T, Meyer CA, et al. Model-based analysis of ChIP-Seq (MACS). *Genome Biol*. 2008;9(9):R137. doi:10.1186/gb-2008-9-9-r137
 53. Schmitt AD, Hu M, Jung I, et al. A compendium of chromatin contact maps reveals spatially active regions in the human genome. *Cell Rep*. 2016;17(8):2042-2059. doi:10.1016/j.celrep.2016.10.061
 54. Ren B, Yang J, Wang C, et al. High-resolution hi-C maps highlight multiscale 3D epigenome reprogramming during pancreatic cancer metastasis. *J Hematol Oncol*. 2021;14(1):1-19. doi:10.1186/s13045-021-01131-0
 55. Lee KM, Yasuda H, Hollingsworth MA, Ouellette MM. Notch2-positive progenitors with the intrinsic ability to give rise to pancreatic ductal cells. *Lab Invest*. 2005;85(8):1003-1012. doi:10.1038/labinvest.3700298
 56. Sungalee S, Liu Y, Lambuta RA, et al. Histone acetylation dynamics modulates chromatin conformation and allele-specific interactions at oncogenic loci. *Nat Genet*. 2021;53(5):650-662. doi:10.1038/s41588-021-00842-x
 57. Dixon JR, Jung I, Selvaraj S, et al. Chromatin architecture reorganization during stem cell differentiation. *Nature*. 2015;518(7539):331-336. doi:10.1038/nature14222
 58. Bhat P, Honson D, Guttman M. Nuclear compartmentalization as a mechanism of quantitative control of gene expression. *Nat Rev Mol Cell Biol*. 2021;22(10):653-670. doi:10.1038/s41580-021-00387-1
 59. Hua H, Zhang YQ, Dabernat S, et al. BMP4 regulates pancreatic progenitor cell expansion through Id2. *J Biol Chem*. 2006;281(19):13574-13580. doi:10.1074/jbc.M600526200
 60. Lau J, Kawahira H, Hebrok M. Hedgehog signaling in pancreas development and disease. *Cell Mol Life Sci*. 2006;63(6):642-652. doi:10.1007/s00018-005-5357-z
 61. Grubert F, Srivas R, Spacek DV, et al. Landscape of cohesin-mediated chromatin loops in the human genome. *Nature*. 2020;583(7818):737-743. doi:10.1038/s41586-020-2151-x
 62. Sharma R, Choi KJ, Quan MD, et al. Liquid condensation of reprogramming factor KLF4 with DNA provides a mechanism

- for chromatin organization. *Nat Commun.* 2021;12(1):5579. doi:10.1038/s41467-021-25761-7
63. Chen X, Shen Y, Draper W, et al. ATAC-seq reveals the accessible genome by transposase-mediated imaging and sequencing. *Nat Methods.* 2016;13(12):1013-1020. doi:10.1038/nmeth.4031
64. Clissold RL, Hamilton AJ, Hattersley AT, Ellard S, Bingham C. HNF1B-associated renal and extra-renal disease - an expanding clinical spectrum. *Nat Rev Nephrol.* 2015;11(2):102-112. doi:10.1038/nrneph.2014.232
65. Van Der Lee R, Buljan M, Lang B, et al. Classification of intrinsically disordered regions and proteins. *Chem Rev.* 2014;114(13):6589-6631. doi:10.1021/cr400525m
66. Banani SF, Lee HO, Hyman AA, Rosen MK. Biomolecular condensates: organizers of cellular biochemistry. *Nat Rev Mol Cell Biol.* 2017;18(5):285-298. doi:10.1038/nrm.2017.7
67. Shin Y, Brangwynne CP. Liquid phase condensation in cell physiology and disease. *Science.* 2017;357(6357). doi:10.1126/science.aaf4382
68. Çubuk H, Yalçın ÇÖ. A review of functional characterization of single amino acid change mutations in HNF transcription factors in MODY pathogenesis. *Protein J.* 2021;40(3):348-360. doi:10.1007/s10930-021-09991-8
69. Li W, Hu J, Shi B, et al. Biophysical properties of AKAP95 protein condensates regulate splicing and tumorigenesis. *Nat Cell Biol.* 2020;22(8):960-972. doi:10.1038/s41556-020-0550-8
70. Dolgin E. Drug startups coalesce around condensates. *Nat Biotechnol.* 2021;39(2):123-125. doi:10.1038/s41587-021-00828-4
71. Boija A, Klein IA, Young RA. Biomolecular condensates and cancer. *Cancer Cell.* 2021;39(2):174-192. doi:10.1016/j.ccell.2020.12.003

SUPPORTING INFORMATION

Additional supporting information can be found online in the Supporting Information section at the end of this article.

How to cite this article: Kato H, Tateishi K, Iwadate D, et al. HNF1B-driven three-dimensional chromatin structure for molecular classification in pancreatic cancers. *Cancer Sci.* 2023;114:1672-1685. doi:10.1111/cas.15690